Acta Materialia 124 (2017) 290–304

Contents lists available at ScienceDirect

Acta Materialia

journal homepage: www.elsevier.com/locate/actamat

Full length article

A synchrotron X-ray diffraction study of non-proportional strain-path effects

D.M. Collins [a, *], T. Erinosho [b], F.P.E. Dunne [c], R.I. Todd [a], T. Connolley [d], M. Mostafavi [b], H. Kupfer [e], A.J. Wilkinson [a, 1]

[a] Department of Materials, University of Oxford, Parks Road, Oxford, OX1 3PH, UK
[b] Department of Mechanical Engineering, University of Bristol, Queen's Building, University Walk, Bristol, BS8 1TR, UK
[c] Department of Materials, Imperial College London, Exhibition Road, London, SW7 2AZ, UK
[d] Diamond Light Source Ltd, Harwell Science & Innovation Campus, Didcot, OX11 0DE, UK
[e] BMW Group, Technology Metal Dingolfing, Landshuter Straße 56, 84130, Dingolfing, Germany

ARTICLE INFO

Article history:
Received 7 May 2016
Received in revised form
31 October 2016
Accepted 5 November 2016
Available online 14 November 2016

Keywords:
Synchrotron radiation
X-ray diffraction (XRD)
Lattice strain
Texture
Crystal plasticity

ABSTRACT

Common alloys used in sheet form can display a significant ductility benefit when they are subjected to certain multiaxial strain paths. This effect has been studied here for a polycrystalline ferritic steel using a combination of Nakajima bulge testing, X-ray diffraction during biaxial testing of cruciform samples and crystal plasticity finite element (CPFE) modelling. Greatest gains in strain to failure were found when subjecting sheets to uniaxial loading followed by balanced biaxial deformation, resulting in a total deformation close to plane-strain. A combined strain of approximately double that of proportional loading was achieved. The evolution of macrostrain, microstrain and texture during non-proportional loading were evaluated by in-situ high energy synchrotron diffraction. The results have demonstrated that the inhomogeneous strain accumulation from non-proportional deformation is strongly dependent on texture and the applied strain-ratio of the first deformation pass. Experimental diffraction evidence is supported by results produced by a novel method of CPFE-derived diffraction simulation. Using constitutive laws selected on the basis of good agreement with measured lattice strain development, the CPFE model demonstrated the capability to replicate ductility gains measured experimentally.

1. Introduction

A number of metallic alloy systems have been reported to exhibit a significant ductility benefit when they are subjected to a non-proportional strain-path [1–4]. Such deformation routes typically involve a first loading path up to a fixed plastic strain followed by further deformation at a different strain ratio. Whilst this effect has been known for some time, experimental studies to date have failed to identify why a metallic material may display such behaviour and capture the behaviour in a microstructural model. Exploiting this benefit, particularly in sheet fabrication processes, may offer significant processing advantages – allowing more complex shapes and structures to be achieved than would otherwise be possible using proportional strain-paths.

To ascertain the ductility of a sheet-formed material, a forming limit diagram may be constructed to determine the range of in-plane principal strains that can be withstood by a sheet of metal without the presence of localised thinning and failure [5]. Data are typically obtained from bulge testing, where Nakajima testing [6] is perhaps the most common. Critically, the strain-ratio of the test can be varied by modification of the specimen geometry; enabling a wide range of strain states to be tested that replicate the possible conditions a component will be subjected to during sheet fabrication. Understanding the formability of a material is particularly important in the automotive industry, where the fabrication of high strength steels at room temperature remains essential to the manufacture of many components. The material will be subjected to various strain-ratios that vary with location within the sheet; in some areas reaching high plastic strains up to 20–30%. These loading conditions of a cold forming process in steels can give rise to necking and thereby localised thinning, leading eventually to

* Corresponding author.
E-mail address: david.collins@materials.ox.ac.uk (D.M. Collins).
[1] Prof. A.J. Wilkinson was an Editor of the journal during the review period of the article. To avoid a conflict of interest, Irene Beyerlein acted as Editor for this manuscript.

http://dx.doi.org/10.1016/j.actamat.2016.11.011

ductile failure [7], which is unacceptable in component manufacture. Therefore, understanding the precise strain-ratio dependent ductility limit is critical. If manufacturers are to adopt non-linear strain-paths to increase the obtainable ductility, it is critical that the underlying micromechanical material response is well understood to reliably predict the new forming limits.

Various studies have been performed on different strain-paths; each identifying a unique, strain-path dependent, macroscopic response. The non-proportional deformation of brass and interstitial free steel, when given a plane-strain pre-strain followed by uniaxial tension, has shown different rates of work hardening influenced by the pre-strain compared to simple uniaxial loading without a pre-strain [8]. Other strain-paths including pre-shear followed by further shear deformation on another plane [9,10] and tension-shear sequences [11] have also been investigated. The latter suggested the accumulation of deformation in the second deformation step was dependent on the activation of slip systems with the highest Schmid factor that were previously latent during the pre-strain [11]. Strain-path dependent hardening behaviour has been shown to directly influence the evolution of dislocation structures [12]. The nature of hardening itself was modelled by Erinosho et al. [13,14], demonstrating that self and isotropic latent rules of hardening influence the density of dislocations produced in different texture components. Furthermore, the study showed that the degree of non-proportionality affects strain localisation, ultimately limiting ductility. The abruptness of a strain-path change has also been shown to have a dramatic effect on the macroscopic stress response [15].

Non-proportional deformation including multiaxial stress-states have been studied by a number of investigators using diffraction-based methods. Repper et al. [16] performed the first in-situ neutron diffraction on cruciform specimens. Both proportional and non-proportional strain-paths have been investigated by Van Petegem et al. [17] using in-situ neutron diffraction. Measurements showed that the accumulated intergranular strains are strongly dependent on the applied stress state. The study also found that subjecting the material to a 90° change in strain-path produced transient softening from measurement of internal strain recovery and micro yielding. Transient softening was also observed by Gonzalez et al. [18] when subjecting an austenitic stainless steel to a 90° strain-path change. X-ray diffraction has also been used to study the evolution of deformation under multi-axial loading [19,20]. Stress-strain [21] curves and the evolution of yield loci [22] under multiaxial stress states have been obtained from the "$\sin^2\psi$" method from X-ray diffraction experiments. Such methods can also be used to measure multi-axial strain fields from Marciniak punch tests [23]. Furthermore, X-ray diffraction methods have enabled assessment of dislocation structure evolution during non-proportional deformation, including observations from peak broadening [17] and dislocation cell structures size measurement from three-dimensional reciprocal space mapping [24]. Modelling studies including a finite-element and fast Fourier transform method [25] and a crystal-plasticity finite element method [26] have demonstrated that calculated lattice strains from such simulations can replicate experimental measurements of lattice strains with good agreement.

In a previous study of proportional biaxial deformation using high-energy synchrotron X-ray diffraction, a technique was developed that allows the micromechanics of a material to be studied in-situ, whilst subjecting sheets to strain-paths with a fixed strain ratio [20]. This revealed that the angular distribution of lattice-strain magnitudes that accumulates during testing is highly sensitive to the given strain-path. This testing method additionally permits the evolution of texture to be assessed. In the current study, the previous testing methodology is replicated to investigate the effect of non-proportional strain-paths in a low-carbon ferritic steel, denoted as DX54. Firstly, the effect of non-proportionality is described for this material from a matrix of Nakajima tests. These results are used to select a subset of experimental strain-paths to be studied in further detail, using in-situ X-ray diffraction. The hardening and texture evolution is then directly compared to simulations made using crystal-plasticity finite element modelling. Finally, the model that best replicates the X-ray diffraction response is used to predict the ductility of selected Nakajima strain-paths, and hence the ductility gain that is displayed by certain non-proportional deformation paths.

2. Experimental method

A single phase ferritic steel with a nominal chemical composition shown in Table 1, denoted as DX54 [27], has been examined in this study. Prior EBSD measurements showed the material exhibits a mean grain size of ~20 μm with an approximately equiaxed morphology [20]. The material had been previously cold rolled to a thickness of ~1 mm and galvanised. The rolling direction, RD, is used as the reference orientation hereon for all subsequent deformation performed.

Non-proportional strain-paths were given to steel specimens by first subjecting the material to either a uniaxial or biaxial pre-strain. Photographs of the specimen geometry and example digital image correlation (DIC) maps that measure the in-plane macroscopic strains are shown in Fig. 1. The biaxial pre-strain was achieved by deforming the material with a flat punch to achieve a region of uniform plastic strain sufficiently large to cut Nakajima test specimens for subsequent deformation. Similarly, uniaxial pre-strains were achieved by loading a sheet along a single axis, constraining the sheet with clamps in one direction, and unconstrained perpendicular.

Nakajima bulge testing was conducted on the pre-strained material to measure the failure strain from a number of non-proportional strain-paths. A hemispherical punch was driven into the plane normal of sheet blanks at a constant rate of 40 mm min^{-1} (strain-rate ~1 × 10^{-2} s^{-1}), deforming an area constrained by a fixed circular hoop with an inner diameter of 150 mm. These tests were performed on sheets that had been subjected to either a deformation under a uniaxial pre-strain or a balanced biaxial pre-strain up to a predetermined plastic strain. Images of a speckle pattern deposited onto the sample surface were acquired at a frame rate of 1/3 Hz throughout the deformation. Post-processing of these images using digital image correlation (DIC) provides the in-plane major, ε_1, and minor, ε_2, true strains.

A high energy X-ray diffraction experiment was next performed on the I12 beamline at the Diamond Light Source [29]. Diffraction patterns were collected at a frame rate of 0.25 Hz whilst deforming cruciform samples, enabling the dynamic micrcomechanical response to be analysed. The deformation was controlled by a purpose built biaxial loading mechanism that has the freedom to test sheet metallic material to high plastic strains along a wide range of biaxial strain ratios; analogous to strain-paths achievable in real fabrication processes. Further details of the biaxial loading mechanism and cruciform specimen design are described in Ref. [20]. Of note, is a locally thin disc-shaped region at the centre of the specimen, symmetric through the thickness, where the X-ray

Table 1
Composition of the ferritic steel, DX54 [28].

Element	Fe	C	P	S	Mn
wt.%	balance	≤0.06	≤0.025	≤0.025	≤0.35

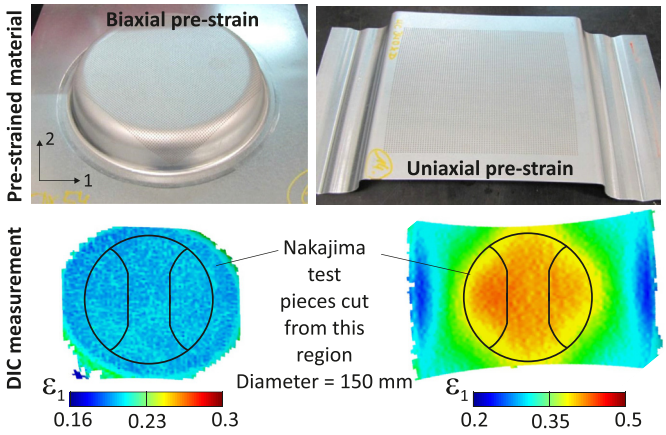

Fig. 1. Photographs of pre-strained material geometries with example macroscopic strain maps shown below, measured from DIC, with approximate location of Nakajima test specimens cut for subsequent deformation.

beam penetrates. This region had dimensions of approximately 400 μm thick (sample to sample variation was approximately ± 50 μm) and a diameter of 6 ± 0.1 mm. The biaxial mechanism was fitted to a Shimadzu AGS-X 10 kN load frame to actuate the deformation mechanism, and was subsequently placed onto a sample stage at the I12 beamline.

Three dissimilar strain-paths were selected for investigation during the available beam time. These are shown schematically in Fig. 2. Samples were deformed under displacement control at a rate of 0.04 mm s^{-1}. The strain rate in the gauge volume was dependent on the distribution of plastic strain across the whole sample, changing for different strain-ratios. However, this was approximately in the range 1×10^{-5} s^{-1} to 5×10^{-5} s^{-1}. Strain-Path 1 comprises a uniaxial loading step with its tensile axis parallel to the transverse direction (TD), followed by a second uniaxial loading step with the tensile axis parallel to the rolling direction (RD). For uniaxial strain-paths, the samples were gripped in the vertical, loading direction and left ungripped and unconstrained perpendicular to the load axis. The samples were allowed to contract perpendicular to the tensile axis due to Poisson's effect. Strain-Path 2 investigates balanced biaxial deformation followed by uniaxial loading (tensile axis parallel to TD) with a target that the final

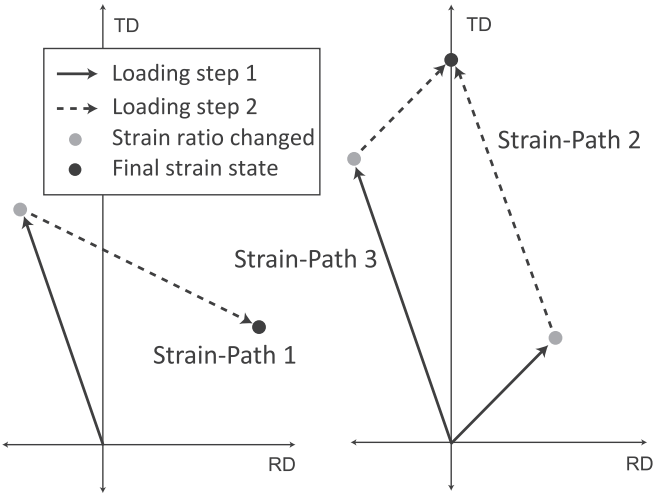

Fig. 2. Schematic illustration of the target non-proportional strain-paths examined experimentally.

deformation state will approximate plane strain parallel to TD. Strain-Path 3 investigates a uniaxial deformation pre-strain followed by balanced biaxial deformation to give a final macroscopic strain state similar to Strain-Path 2.

On the I12 beamline, the samples were positioned ~1125 mm from a Thales Pixium RF4343 2D area detector with a pixel size of 148 μm × 148 μm on a 2880 × 2881 X-ray sensitive array, permitting the acquisition of Debye-Scherrer diffraction rings in transmission. An illustration of this experimental setup is shown in Fig. 3. The monochromatic X-ray beam used was calibrated using a method described by Hart et al. [30] to have an energy of 90.36 keV ($\lambda = 0.1372$ Å) with a CeO_2 standard and had an incident beam size of 0.5 mm × 0.5 mm.

The collected diffraction patterns were radially integrated into 36 sectors of equal spacing using the software FIT2D [31]. Sector one corresponds to an azimuthal angle of $\psi = 0° \pm 5°$ with sector 10 at $\psi = 90° \pm 5°$. These sectors correspond to either ε_{RD} & ε_{TD} or ε_{TD} & ε_{RD}, depending on the sample orientation relative to the detector. Labels are provided in the results to state the orientation of the sheet. Full diffraction rings up to $N = 10$ (where $N = h^2+k^2+l^2$) were collected. Data analysis fitting routines were performed using MATLAB, with each of these reflections fitted with a pseudo-Voigt fitting function. For each fitted reflection, the lattice strain and integrated reflection intensity were monitored. Lattice strains were calculated using Equation (1),

$$\varepsilon_{hkl} = \frac{d - d_0}{d_0} \tag{1}$$

where ε_{hkl} is the lattice strain for the reflection hkl, d_0 is the relaxed reference d-spacing, and d is the measured d-spacing.

Measurements of the macroscopic strain during the

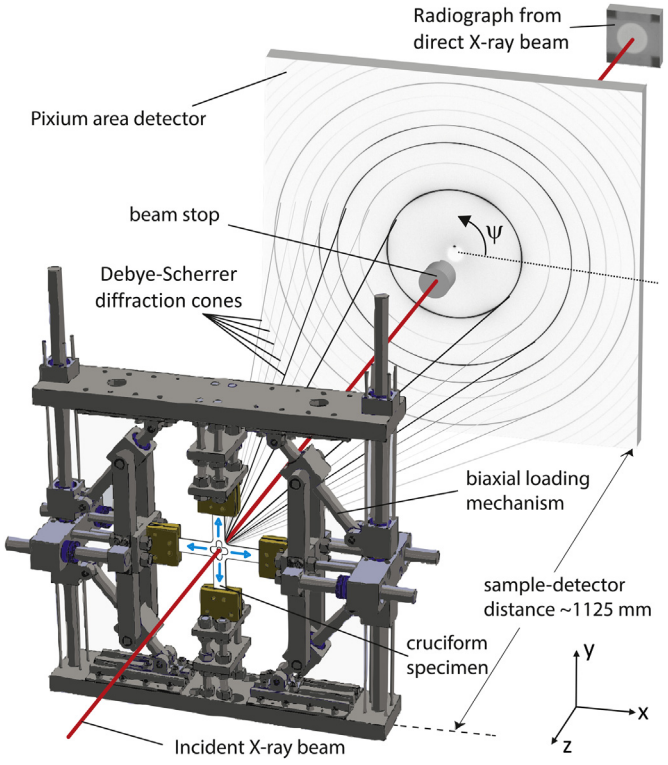

Fig. 3. Experimental setup at the I12 beamline, Diamond Light Source, illustrating the diffraction data acquired from the deforming cruciform specimen. Image adopted from Ref. [26].

deformation were obtained from radiographic images. The radiographs captured a 10 mm × 10 mm selected area near the centre of the specimen. The central thinned region of the specimen had a lower X-ray attenuation compared to the surrounding thicker specimen, and was clearly visible with differing contrast when observed in 461 × 461 pixel 8 bit radiographs obtained with an imaging camera (Fig. 3, top-right). The images were acquired at ~5 mm stroke displacement intervals throughout the deformation to monitor the change in macroscopic strain. Post-processing of these images using an affine transformation and DIC methods were used to measure strain compared to a reference image obtained prior to any applied load. Details of the DIC algorithm used are described in Ref. [32] and experimental method in Ref. [20].

3. Crystal plasticity modelling

3.1. Model outline

To aid the understanding of the experimental non-proportional deformation behaviour, crystal plasticity finite element (CPFE) simulations were performed on strain-paths similar to those measured. These strain-paths of interest are shown schematically in Fig. 4. Each path has two increments comprising either nominally uniaxial loading and/or biaxial deformation. For nominally uniaxial loading, a true strain increase of 0.1 is prescribed parallel to either RD or TD (with the orthogonal axis unconstrained) and for biaxial deformation, a true strain increase of 0.1 is given in both RD and TD. Strain-Paths 1,2 & 3 (experiment) can be compared to paths A, B & C, respectively. To study the influence of the major strain axis with respect to the sheet orientation, simulations for these strain-paths were repeated with the uniaxial components in the orthogonal direction. Thus, path D follows uniaxial (ε_{RD}) + (ε_{TD}) deformation, and is compared to path A; uniaxial (ε_{TD}) + (ε_{RD}). In a similar manner, paths E and F can be compared to paths B and C, respectively.

Crystal plasticity finite element (CPFE) modelling has been used to predict the nature of the deformation response at the grain scale during non-proportional loading. A brief description of the classical crystal plasticity framework that is used in this study is given below. It is based upon a kinematic decomposition of the deformation gradient, $\mathbf{F}$, into elastic $\mathbf{F}^*$ and plastic $\mathbf{F}^p$ tensors as described by Lee [33], where

$$\mathbf{F} = \mathbf{F}^*\mathbf{F}^p \tag{2}$$

Full details on this method are given by Erinosho et al. [13,14]. In this study, a power law constitutive relationship is adopted to relate the slip rate to the resolved shear stress for an individual slip system, as given by

$$\dot{\gamma}^\alpha = \dot{\gamma}_0^\alpha \left|\frac{\tau^\alpha}{g^\alpha}\right|^n \mathrm{sgn}(\dot{\gamma}) \tag{3}$$

where the slip rate, $\dot{\gamma}^\alpha$ on a slip system, α, is dependent on a reference strain rate, $\dot{\gamma}_0^\alpha$, the resolved shear stress, τ^α, and the slip system strength g^α. For further details, the reader is referred to [34,35]. The dislocation hardening law follows McDowell and McGinty [7], describing the evolution of the slip system strength via

$$\dot{g}^\alpha = h_0\left(1 + \frac{h_0\gamma_{\mathrm{sum}}}{\tau_0 m}\right)^{m-1}\dot{\gamma}^\alpha \tag{4}$$

where the accumulated slip, γ_{sum}, is calculated from

$$\gamma_{\mathrm{sum}} = \sum_{\beta=1}^{N_{\mathrm{slip}}}\left(\int_0^t \dot{\gamma}\mathrm{d}t\right) \tag{5}$$

The hardening modulus, h_0, and constant, m are material dependent properties. For each slip system, α, the dislocation density, ρ, is given by

$$\rho^\alpha = \int_0^t \dot{\rho}^\alpha \mathrm{d}t \tag{6}$$

Finally, the relationship between the slip system strength and the dislocation density follows

$$g^\alpha = g_0 + \beta\sqrt{\rho^\alpha} \tag{7}$$

where the initial slip system strength is g_0 and β is a constant.

The parameters used in this study are as follows; $n = 40$; $\dot{\gamma}_0 = 1\,s^{-1}$; $m = 0.245$; $E = 211$ GPa; $\nu = 0.3$; $\tau_0 = 110$ MPa; $h_0 = 0.9$ GPa. These parameters have been determined from experimental results of the DX54 ferritic steel material [27]. This material typically has a yield stress σ_y of 140–185 MPa and an ultimate tensile strength, $\sigma_{UTS} \geq 270$ MPa. The polycrystal model used comprises 8 × 8 × 8 grains with a uniform mesh refinement containing 6 × 6 × 6 elements per grain. It is noted that the total 512 grains modelled is a significant simplification of the number of grains in the diffraction volume (>20,000 assuming spherical grains in the probed volume).

Two types of hardening have been investigated; isotropic latent hardening and self hardening. For isotropic hardening, all slip systems undergo the same level of hardening, irrespective of them being active. The resistance to slip is set equal for all slip systems and will correspond to the maximum resistance currently experienced by any slip system. The term $\dot{\gamma}^\alpha$ in Equation (4) will exhibit the maximum slip rate developed by any slip system, $\dot{\gamma}_{\mathrm{max}}$, for all slip systems. Self hardening allows slip systems to hardening independently, permitting only slip systems that are active to undergo hardening. Here, $\dot{\gamma}^\alpha$ in Equation (4) is dependent on the rate of slip for each slip system, and the total accumulated slip is the sum of all slip systems.

Planar boundary conditions with surface normals along z were unconstrained, while displacements were imposed for the boundary with normal along y to match the vertical strain. The final boundary, with normal along x, was left unconstrained for uniaxial loading, but otherwise had displacements prescribed to match the other component of the imposed in-plane strain. The

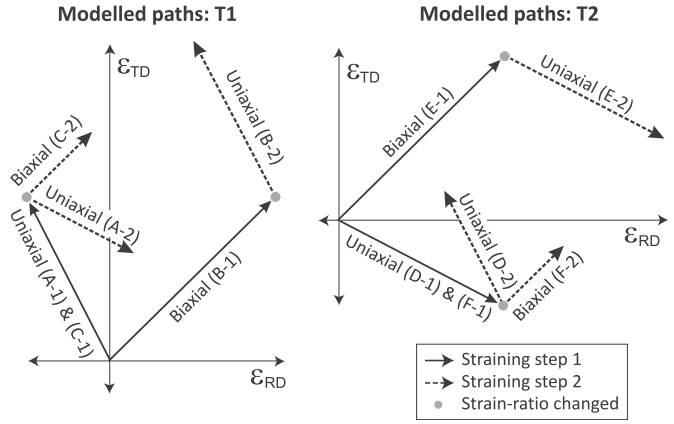

Fig. 4. Non-proportional strain-paths simulated with CPFE with respect to the strain magnitude in the rolling and transverse directions.

displacements prescribed were equivalent to the strains measured via DIC analysis of experimental radiographs in the horizontal and vertical directions. This approach ensured the model was subjected to the equivalent deformations as the circular gauge in the cruciform specimens.

3.2. Simulating diffraction results

To produce results comparable to the experimental diffraction measurements, a previously developed framework [26] to generate diffraction reflections from CPFE simulations has been used. From knowledge of the incident X-ray beam direction and crystal orientation at each integration point within the simulated polycrystal, the associated lattice spacing is calculated if Bragg's law is satisfied within a given tolerance for each of the experimentally observed reflections. For each lattice plane, *hkl*, the plane normal vector, $\mathbf{r}_{hkl}$ to describe its crystallographic orientation is given by

$$\mathbf{r}_{hkl} = \Delta\mathbf{R}^{\mathbf{c}}\mathbf{R}_0^c(hkl) \tag{8}$$

where $\mathbf{R}_0^c$ is the rotation matrix of the undeformed crystal from the reference state to the local crystallographic orientation and $\Delta\mathbf{R}^{\mathbf{c}}$ transforms the crystal orientation into the deformed state. For diffraction to occur, Bragg's law must be satisfied where the Bragg angle, θ_b is satisfied through

$$\theta_b = \sin^{-1}\left(\frac{\lambda}{2d_{hkl}}\right) \tag{9}$$

where λ is the incident wavelength (as calibrated from the synchrotron experiment), and d_{hkl} is the interplanar spacing (determined from the orthogonal lattice vectors calculated within the CPFE simulation). Whether each integration point satisfies the Bragg law will depend on the angle, θ_0, between the lattice vector, $\mathbf{r}_{hkl}$ and its forward projection $\mathbf{s}_0$, given by

$$\mathbf{s}_0 = \begin{bmatrix} r_{hkl_x} \\ r_{hkl_y} \\ 0 \end{bmatrix} \tag{10}$$

where r_{hkl_x} and r_{hkl_y} are the *x* and *y* components (directions shown in Fig. 3) of $\mathbf{r}_{hkl}$, respectively. The lattice plane will diffract when $\theta_b = \theta_0$. Experimentally, this condition is somewhat relaxed by the intrinsically broadened line profile due to instrumental effects and artifacts. Specifically, the broadening arises from a combination of a finite incident X-ray bandwidth, angular resolution limits imposed by the detector pixel size, and any mosaic spread from the sample due to dislocation substructures present. The Bragg angle, θ_b, in reality has a narrow range (approximately 0.02°; the full width at half maximum of a {110} reflection) for which diffraction is allowed. This range may be widened for the simulations, mitigating the issue of few grains diffracting from the limited number of crystals modelled. The condition used in the study was $\theta_b - 5° < \theta_0 < \theta_b + 5°$. The selection of this parameter is discussed in Ref. [36]. If satisfied, $\mathbf{s}_0$ represents the position of the diffraction spot on a virtual area detector. The azimuthal angle, ψ, equivalent to the experimental definition is simply

$$\psi = \tan^{-1}\left(\frac{r_{hkl_y}}{r_{hkl_x}}\right) \tag{11}$$

This calculation was repeated for each integration point to yield the simulated Debye-Sherrer diffraction rings. Thus, a subset of the information calculated from the CPFE model is captured in a similar manner to the experiment. The symmetry of the simulation necessitates azimuthal range of $\psi = 0°$ to $\psi = 180°$ to be calculated. Subsequently, the diffraction rings were radially integrated into 18 sectors with a 10° angular range. For the most statistically reliable data, the {310} reflection was simulated, as it has the highest multiplicity of the experimentally observed reflections. Lattice strain for each sector is also calculated in comparison to the ideal reference, again in the equivalent manner to the experiment using Equation (1). A formal description of this calculation is given in Ref. [26].

A texture prior to deformation of the DX54 material was measured using EBSD, and numerically simulated to seed the CPFE model with representative crystal orientations. Pole figures of the experimentally measured and simulated texture are shown in Fig. 5. Small differences are observed between the simulated and measured texture. This is expected from the sampling effect of 8 × 8 × 8 (512) simulated grains compared to ~2000 grains measured with EBSD.

3.3. Predicting failure strains

A strain limit prediction method previously described by Erinosho et al. [14] at the grain scale in CPFE, based on methods developed by others at the homogenised continuum level, was used to determine forming limit diagrams [37,38]. Material failure is obtained from a macroscopic strain limit criterion corresponding to a threshold level of plastic strain localisation within the grains. A normalised increment of plastic strain, $\widehat{q}_j^t$, for each time step ($t = t_1, t_2, \ldots, t_n$) and grain *j* is calculated for the average plastic strain within the grain, $\mathrm{d}q_j^t$, with respect to the change in average macroscopic plastic strain change, $\mathrm{d}\overline{p}^t$, where

$$\widehat{q}_j^t = \frac{\mathrm{d}q_j^{t_1}}{\mathrm{d}\overline{p}^{t_1}}, \frac{\mathrm{d}q_j^{t_2}}{\mathrm{d}\overline{p}^{t_2}}, \ldots, \frac{\mathrm{d}q_j^{t_n}}{\mathrm{d}\overline{p}^{t_n}} \tag{12}$$

A failure parameter, $\overline{T}$, is introduced that describes the mean plastic strain for grains with the highest values of $\widehat{q}_j^t$. Values of $\widehat{q}_j^t$ are ranked and the values of the top N_c grains are averaged, such that

$$\overline{T} = \frac{1}{N_c}\sum_{i=1}^{N_c}\widehat{q}_i^t \tag{13}$$

where $N_c = 5$ in this study. The parameter $\overline{T}$ is calibrated from the known failure strain of a certain strain path. In this study, the failure of a plane strain specimen at $\varepsilon_1 = 0.45$ and $\varepsilon_2 = 0$ was simulated. When this equivalent macroscopic strain was reached in the model,

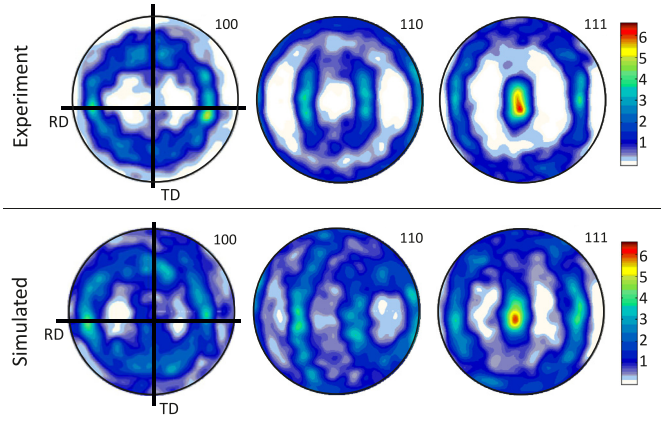

Fig. 5. Experimentally measured and simulated pole figures of the material texture prior to deformation.

the parameter $\overline{T} = 2.5$. For other strain-paths, the macroscopic strain at failure corresponds to this $\overline{T}$ is met.

4. Results

4.1. Nakajima testing

The results of Nakajima testing are shown in Fig. 6. The final strains (at failure) plotted are the total strains in the ε_1 and ε_2 directions from a sum of the measured pre-strain plus the true strain measured with DIC. As a benchmark for ductility, the forming limit curve under proportional deformation conditions is shown. For each non-proportional test, the material had undergone a pre-strain that was either uniaxial loading (U) or biaxial straining (B). The targeted pre-strain magnitude was set to approximately half of strain limit under proportional deformation, similar to those investigated by Nakazima [1] where ductility gains were found. The effect and sensitivity of a pre-strain magnitude to the final ductility possible remains unknown and may be considered in future studies. From the pre-strained material, Nakajima testing was performed to failure with either uniaxial loading (U-a or B-a), plane strain tension (U-b or B-b), biaxial strain, $\varepsilon_2/\varepsilon_1 \approx 0.25$ (U-c or B-c), or balanced biaxial strain, $\varepsilon_2/\varepsilon_1 \approx 1$ (U-d or B-d).

It is shown that certain non-proportional strain-paths reach a plastic strain far greater than is possible if the strain ratio at the final strain state was targeted by proportional loading. For example, consider path U-d, which achieves a plane strain in the major direction of ~0.85 prior to failure. The proportional forming limit shows that under plane strain conditions, a strain of only ~0.42 is reached. Conversely, if the loading operation of path U-d is reversed, such that a biaxial pre-strain is given, followed by uniaxial deformation (i.e. B-a), the final strain state is approximately the same as achieved by proportional plane-strain deformation. This provides clear evidence that the sequence of strain-ratio for each loading step is very important. In other cases, adopting a non-proportional strain-path can be detrimental to ductility. For example path B-b reaches $\varepsilon_1 \approx 0.38$ and $\varepsilon_2 \approx 0.2$, giving a final strain-ratio of $\varepsilon_2/\varepsilon_1 \approx 0.5$. Extrapolating this strain ratio for proportional loading yields $\varepsilon_1 \approx 0.54$ and $\varepsilon_2 \approx 0.29$, which is clearly significantly greater.

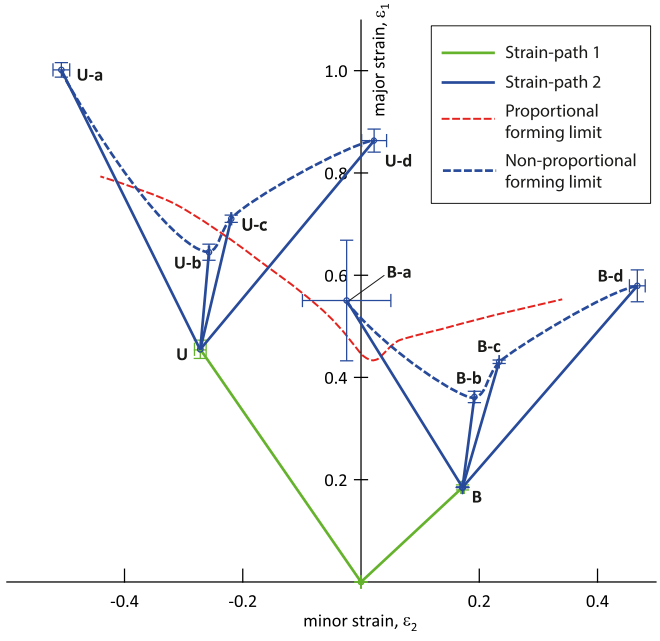

Fig. 6. Forming limit diagram showing the strain to failure for various non-proportional strain-paths in comparison to conventional proportional deformation.

4.2. Diffraction testing – macroscopic strains

The strong dependence of the strain-ratio loading sequence shown in the Nakajima testing results has been investigated further using in-situ deformation of cruciform samples whilst acquiring X-ray diffraction data. The measured macroscopic strain, relative to the original rolling direction (RD) and the transverse direction (TD) accumulated during each deformation path are shown in Fig. 7. For each data point, five radiograph images were acquired and DIC analysis was performed on each. The data points are the mean measurement and the error bars give the standard deviation of these measurements. An alternative analysis was conducted in which a uniform affine transformation was applied to the radiographs of the deformed sample until an optimised match to the initial radiograph of the undeformed sample was obtained.

Referring to Fig. 7, a good correlation is seen between the affine transformation and DIC analysis methods, though the latter measurements tend to return a higher strain magnitude. For consistency with previously published results [20], the affine transformation results are used from here on. In Fig. 7 (a), nominally uniaxial loading is firstly given parallel to TD up to a stroke displacement of 10 mm corresponding to a true strain of 0.1 (TD) and −0.09 (RD). Whilst uniaxial loading was targeted, the specimen geometry provides a greater contraction parallel to RD than would be measured in a truly uniaxial test (with Poisson's ratio of 0.5 expected). Upon changing the tensile axis (the sample is rotated by 90°), now parallel to RD, the direction of strain accumulation reverses. This can be seen more clearly by plotting ε_{TD} versus ε_{RD}, as shown in Fig. 7 (d). Deforming until the stroke displacement reaches 27 mm, passes the condition where the macroscopic strains in RD and TD returns to approximately zero. The final deformation yields a true strain of 0.07 (RD) and 0.02 (TD) at the end of the test.

Strain-Path 2 in Fig. 7 (b) follows a biaxial strain up to 25 mm stroke displacement; reaching strains of 0.09 (RD) and 0.04 (TD) before the strain-path change; giving a strain ratio $\varepsilon_{RD}/\varepsilon_{TD} \approx 1.8$. Whilst balanced biaxial deformation was targeted, greater compliance in the biaxial loading mechanism parallel to TD results in this difference. Following the strain-path change to uniaxial loading with tensile axis parallel to TD, the gradient of true strain RD versus true strain TD is close to that of Strain-Path 1. When the test is stopped, the final true strain reaches −0.04 (RD) and 0.27 (TD), with an overall strain-path plotted in Fig. 7 (d). Strain-Path 3 investigates the effect of switching the strain-ratio loading sequence, so firstly deforming under a uniaxial load before deforming biaxially. The material is initially deformed up to 10 mm stroke displacement parallel to TD, as shown in Fig. 7 (c), equivalent to the initial deformation studied in Strain-Path 1. However, beyond 10 mm stroke displacement when deforming the material in a targeted biaxial manner, further plastic deformation is limited. The stroke displacement increases, providing an increase in the applied force to the sample, though the measured change in ε_{TD} and ε_{RD} is only ~0.01. The reason is due to greater plasticity occurring in the arms of the specimen compared to the gauge volume, with the cruciform design limiting the maximum macroscopic strain that could be achieved. The limited change in plastic strain beyond the strain-path change can be easily seen in Fig. 7 (d).

4.3. Diffraction testing – lattice strain and intensity evolution

For a qualitative comparison of the lattice strains and integrated peak intensity evolution for each non-proportional strain-path, maps of these data have been plotted as a function of azimuthal

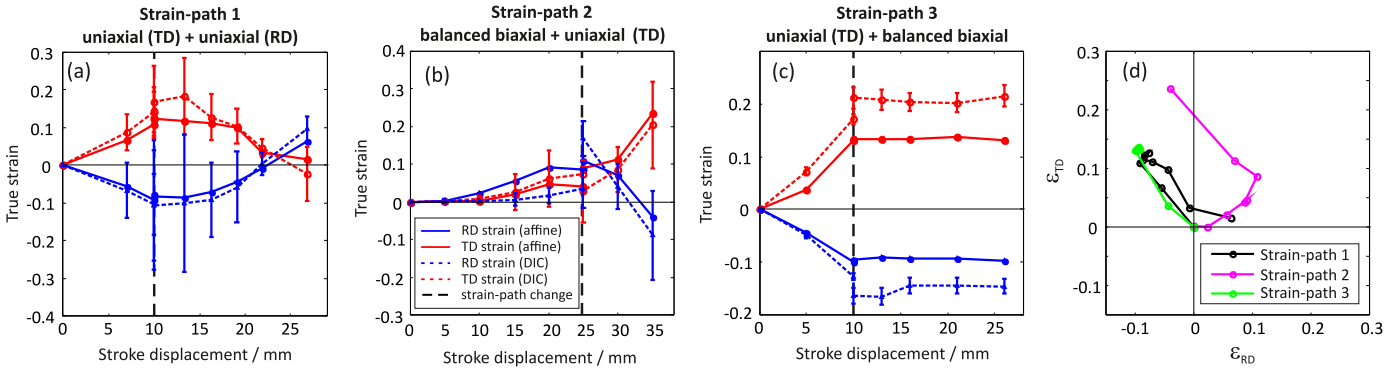

Fig. 7. Measured macrostrain from X-ray radiographs of the experimental non-proportional strain-paths (a–c), and these plotted together with respect to strain in the rolling and transverse directions (d).

angle, ψ, and stroke displacement in Fig. 8. These are presented for the {110}, {200}, {211} and {222} reflections. Note that {310} results are shown later when compared with modelled results (Fig. 11). To assist interpretation of these data, line profiles of the {200} lattice strain versus azimuthal angle are plotted at stroke displacement increments for each strain-path in Fig. 9. For each strain-path, the lattice strain distribution with azimuthal angle and texture development during the first strain-ratio replicates the targeted uniaxial and biaxial deformation trends presented in an earlier study of proportional deformation [20]. The key observations were that the magnitude of lattice strain accumulates most rapidly in the direction of the tensile axis with the highest load, irrespective of the reflection studied. This is most clearly evident in the first loading step for Strain-Paths 1 and 3 where loading is uniaxial. This is also evident during lower plastic strains when the first strain-ratio is biaxial, as shown in Strain-Path 2 when the stroke displacement is less than ~10 mm. This is because of the departure from the targeted balanced biaxial strains, shown in Fig. 7 (b). Evidence of this is also clear in Fig. 9 (b), where the lattice strain distribution is quite similar to the uniaxial deformation lattice strain distribution in Fig. 9 (a). At higher plastic strains, the lattice strain distributes approximately isotropically with respect to azimuthal angle, for example at ~20 mm in Fig. 8(i–l).

Whether the first loading step is uniaxial or biaxial, evidence of a texture change is also clear from plots of integrated intensity; each labelled with $I_{\{hkl\}}$ in Fig. 8. The initial intensity symmetry characteristic of the prior rolling of the as-received material is shown to change for all strain-paths. The {110} reflections during uniaxial loading, for example, initially has a 2-fold intensity symmetry which begins to disappear at ~3 mm to produce a 6-fold symmetry at ~7 mm. This corresponds to a true strain range of 0.028–0.066 by interpolation of the macroscopic strains (Fig. 7). A similar distinct intensity change can be seen for the other reflections shown in Fig. 8 during uniaxial loading as the first deformation step. The intensity changes during biaxial deformation as the first loading step are comparatively subtle, though evidence can be seen for the {222} reflection; where the magnitude of the intensity features at $\psi = 0°$ and $\psi = 180°$ reduces with stroke displacement, as shown in Fig. 8 (p).

Upon changing the strain-path, as indicated by the dashed lines in Fig. 8, the lattice strain and intensity distributions that develop differ significantly from those produced by proportional loading with the equivalent strain ratio. Considering firstly Strain-Path 1 beyond 10 mm stroke displacement, the lattice strain accumulates in a similar manner as the prior uniaxial deformation, though with the highest magnitude now parallel to the new tensile axis (parallel to RD). Evidence of residual elastic strain present from the prior deformation is visible at $\psi = 90°$ and $\psi = 270°$ for the {200} lattice strain measurement; Fig. 8 (b). However, the subsequent accumulation in lattice strain appears unaffected by the prior deformation, i.e. the largest magnitude of lattice strain remains parallel to the tensile axis and compressive perpendicular. Following the strain-path change, the intensity and distribution of each reflection, as shown in Fig. 8(e–h), remains unchanged until ~18 mm stroke displacement. Between the nominal strain-path change and this point, the stroke has been taking up slack in the rig, as shown in the limited increase of macroscopic strain in Fig. 7 (a). The resulting symmetry and intensity subsequently returns to a distribution resembling the initial condition.

From the second load step in Strain-Path 2, the lattice strain accumulates most rapidly in the direction of the tensile axis, TD. For the first few mm of stroke displacement, lattice strain is not accumulated. This is again slack in the rig, accumulating little load in the sample, as shown in Fig. 7 (b). From this, the maximum lattice strain is not reached until an additional ~4 mm stroke displacement has passed beyond the strain path change as shown in Fig. 8(i–l). The observed intensity changes during nominally uniaxial loading in Strain-Path 2 are similar to the pre-strain in Strain-Path 1. The resulting intensity distribution/symmetry, for all reflections studied, is characteristic of each test that includes uniaxial loading. A significant intensity change does not occur over a wide stroke displacement range, instead developing over a narrow increment in stroke displacement when the macroscopic strain changes rapidly (~30 mm stroke displacement in Fig. 7 (b)).

Referring to Fig. 8(q–t), the change of strain-ratio in Strain-Path 3 to biaxial deformation after prior nominally uniaxial loading provides a quite different lattice strain distribution compared to those measured when biaxial deformation was the first loading step, i.e. in Strain-Path 2. It is, however, noted that the macroscopic strain increase from biaxial deformation in Strain-Path 3 during this loading is small at ~1%. In the example of a biaxial pre-strain, Fig. 8(i–l), the lattice strain is accommodated quite isotropically with respect to azimuthal angle, whereas after the uniaxial preload, the lattice strain is accumulates to a greater magnitude at azimuthal angles, ψ, close to 0°, 180° & 360° (Fig. 8(q–t)). This is parallel to RD and perpendicular to the loading direction of the pre-strain. At azimuthal angles close to the direction of the pre-strain, TD, at $\psi = 90°$ and $\psi = 270°$, the lattice strain accumulates at a comparably lower magnitude. This trend is observed for all reflections studied. The evolution of lattice strain distribution is also shown in Fig. 9 (f). The intensity change throughout the deformation for each reflection is shown in Fig. 8(u–x). A change is observed in the uniaxial pre-strain, equivalent to Strain-Path 1, however, with the switch in strain-path, the intensity distribution

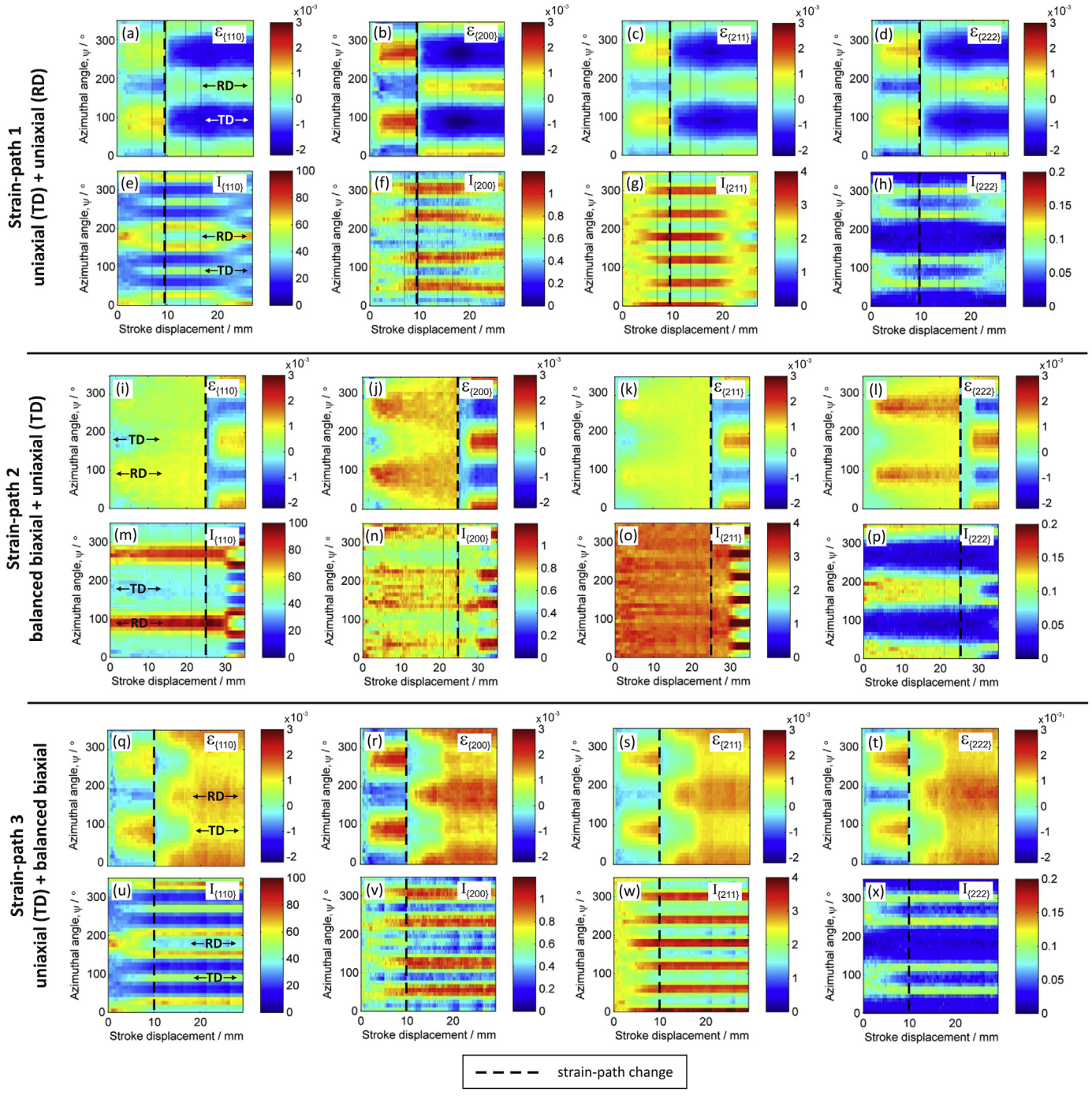

Fig. 8. Lattice strain and integrated reflection intensity of the {110}, {200}, {211} and {222} lattice planes for the experimentally measured non-proportional loading paths.

with azimuthal angle is retained for the remainder of the test. This indicates that no new texture fibre develops throughout this small (~1%) additional plastic strain. After the test was complete, it was evident that the sample had deformed significantly in the cruciform arms, with only limited plastic deformation at the sample centre. In this case, the cruciform design limited the maximum plastic strain achievable at the centre of the specimen during this strain path.

Lattice strains have been plotted for sectors corresponding to the two tensile axis of the biaxial loading mechanism, shown in Fig. 10. Information is obtained from sectors close to $\psi = 0°$ and $\psi = 90°$, shown schematically in (a), corresponding to TD and RD, or, RD and TD (depending on sheet orientation relative to the detector) in the plane of the specimen. Lattice strains are plotted with respect to the macroscopic strain (interpolated from the X-ray radiography measurements) in the transverse direction. The arrows denote the progression of lattice strain with time. Strain-Path 1 in Fig. 10 (b) and (c) show that the magnitudes of lattice strains in the tensile direction, TD for pass 1 and RD for pass 2 are quite different. An initially high work hardening rate is clear in pass 1, particularly when $\varepsilon_{TD} < 0.06$, whereas the lattice strains in pass 2 do not increase significantly with plastic strain beyond the initial elastic

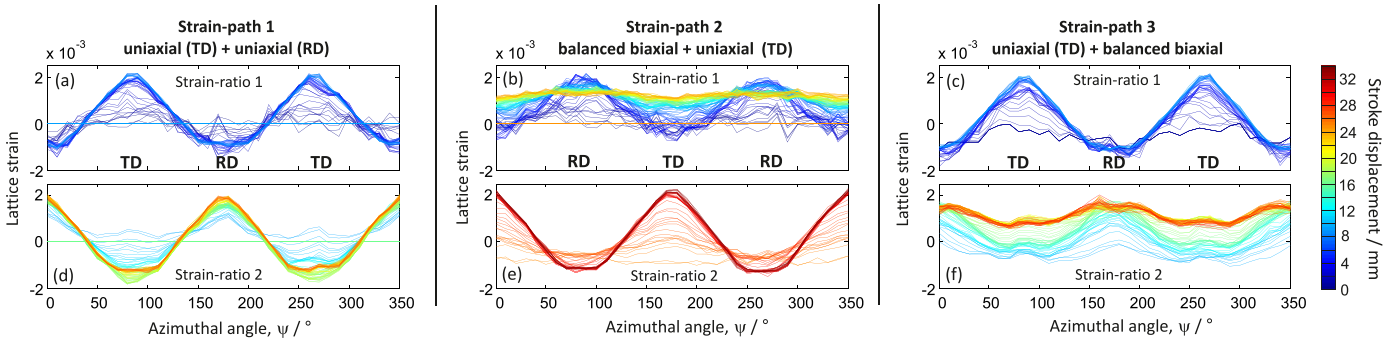

Fig. 9. Evolution of measured {200} lattice strain distributions for different non-proportional strain paths.

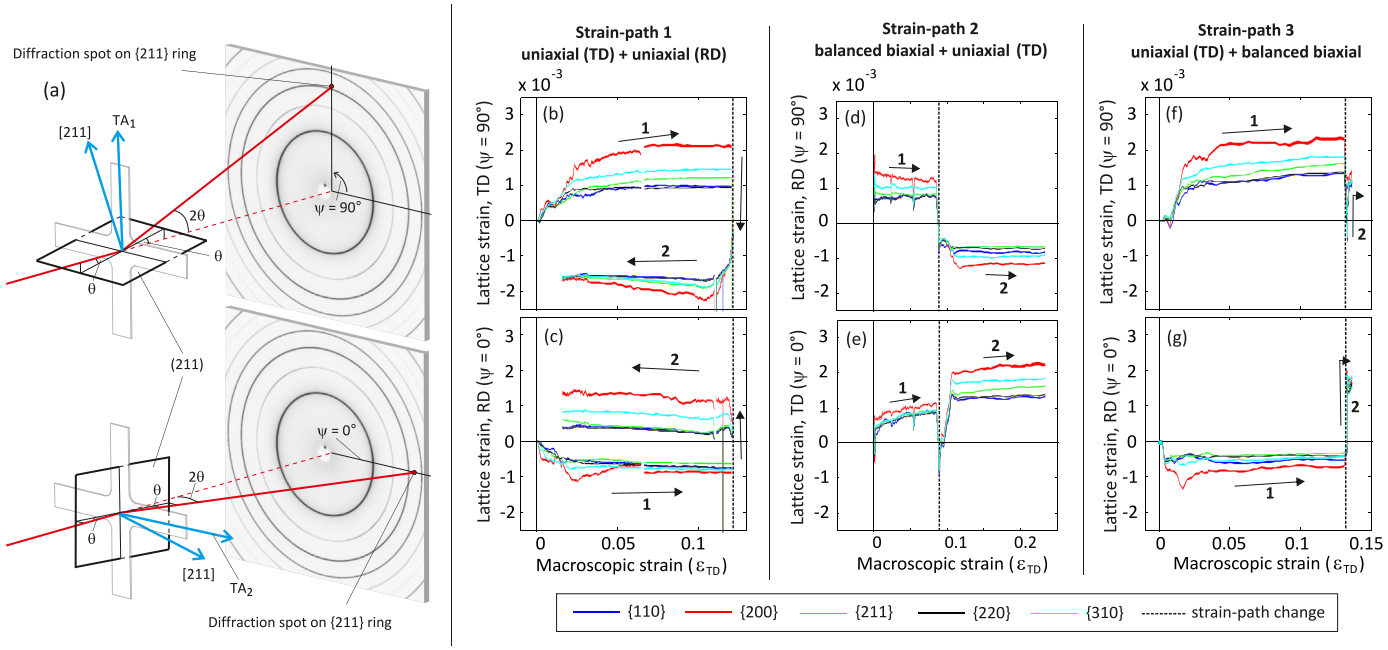

Fig. 10. Lattice strains parallel to two deformation axes ($\psi = 0°$ and $\psi = 90°$) as a function of macroscopic strain in the transverse direction for each non-proportional strain-path investigated.

reloading. Normal to the applied stress (RD pass 1, TD pass 2), the lattice strains are quite uniform (except {200}) with deformation in pass 1, whilst apparent softening is observed in pass 2, which is most pronounced in the {200}.

After the strain-path change in Strain-Path 2, the uniaxial loading in the tensile direction (TD) shows limited work hardening for each reflection shown. In the perpendicular direction (RD), some softening is observed. The softening in this strain-path (after biaxial deformation), is not as significant as Strain-Path 1, which instead had a uniaxial pre-strain. For both Strain-Paths 1 and 2 it is notable that the transverse strains show more dispersion between grain families after the strain-path change than before it.

Beyond the path change in Strain-Path 3, the limited plastic deformation makes interpretation of trends difficult. However, parallel to RD during biaxial deformation, the lattice strains for all reflections are higher than those measured during a biaxial pre-strain (Strain-Path 2). Furthermore, the differences in the magnitude of lattice strain between each reflection are shown to be quite similar, whereas differences between each lattice plane during a biaxial pre-strain vary depending on the single crystal plane specific stiffnesses [39].

4.4. Calculated lattice strains from CPFE models

Simulations have been performed that predict the {310} lattice strain evolution for the strain-paths A-F (Fig. 4) for azimuthal angles $0° \leq \psi \leq 180°$. Results are shown for self and isotropic hardening. Simulations have been made with the major tensile axis identical to the experiment (T1), and with the major tensile axis perpendicular (T2). The latter simulations are simply a repeat of T1 paths, with the deformed sheet rotated by 90° to investigate the effect of initial texture. Results from the modelled lattice strain-maps were calculated at linear displacement increments which have been scaled to be equal to the experimental stroke displacement. A direct comparison between the modelled (T1 paths) and experimental measurements are shown in Fig. 11(a–f) as a function of macroscopic strain at $\psi = 0°$ and $\psi = 90°$. Results are shown for self hardening (a-c) and isotropic hardening (d-f).

In general, there is good agreement between the modelled and experimentally measured lattice strain maps. The colour scales illustrate that the magnitudes of lattice strain simulated from the self hardening model are in better agreement than the isotropic case. For the latter, the lattice strain magnitudes are far higher than

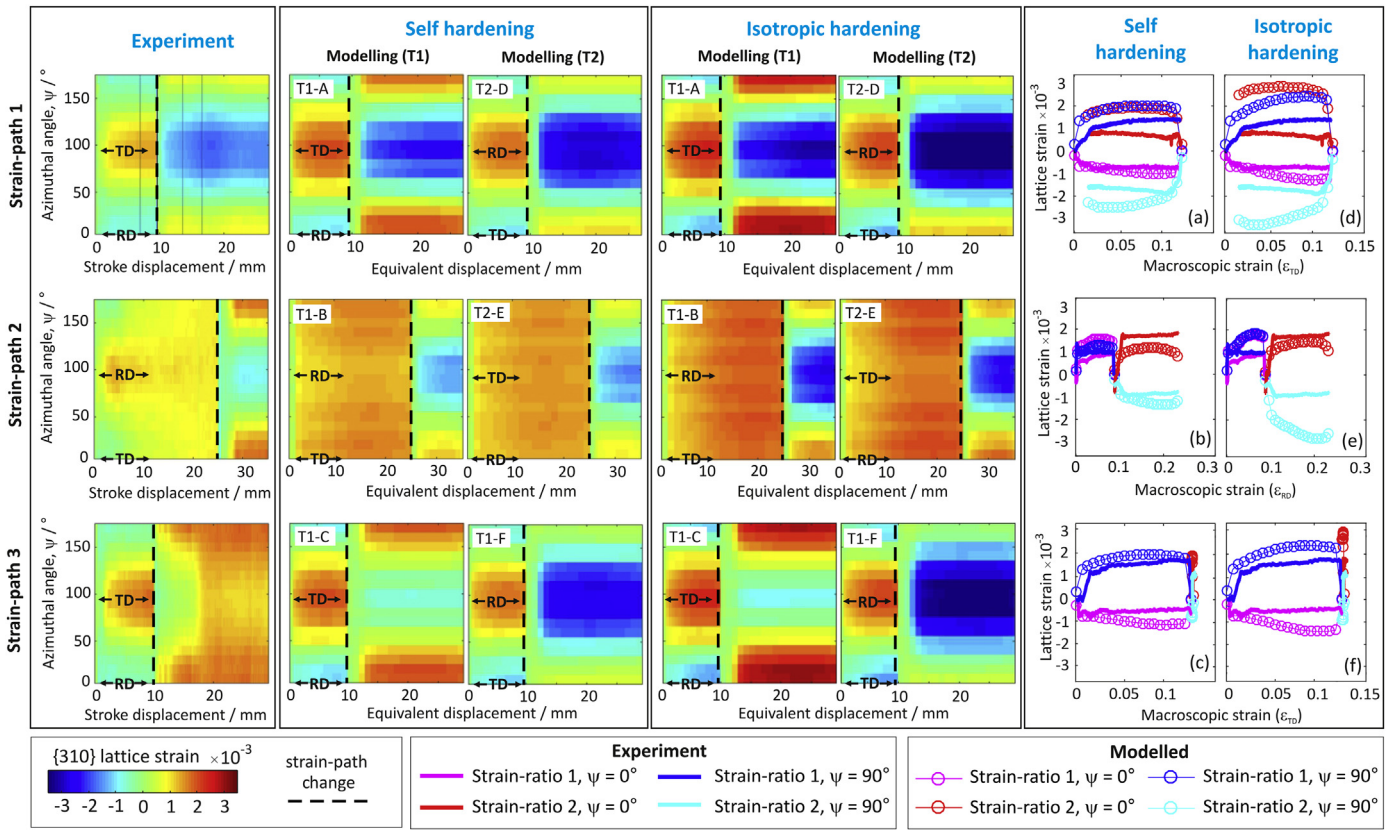

Fig. 11. Simulated {310} lattice strain maps obtained from CPFE simulations for various non-proportional strain-paths using self and isotropic hardening.

those measured; over predicting the measured rate of hardening. The modelled results from Strain-Path 1 (T1-A) provide similar tensile to compressive lattice strain distributions with ψ during the pre-strain and second deformation step, although the lattice strain magnitudes are predicted to be higher than the experimentally measured values, as seen in Fig. 11 (a) & (d), for example. Changing the sheet orientation to T2-D predicts lower absolute values of lattice strain compared to T1-A, indicating that the lattice strain distributions measured must be strongly related to any initial texture. The implication is that the rate of hardening is lower when the sheet is the T2 orientation.

The biased accumulation of {310} lattice strain parallel to RD during initial straining of biaxial deformation in Strain-Path 2 is not replicated by the model. Instead, a uniform distribution of lattice strain with respect to ψ is produced, irrespective of sheet orientation (T1 or T2). Following the strain path change, tensile lattice strains are measured and simulated parallel to the new tensile axis and compressive perpendicular. The model has subjected the material to a fixed stain-ratio during the pre-strain. However, the strain ratio is unlikely to be constant during the experiment, instead favouring strain accumulation parallel to RD initially as slack is taken up in the rig perpendicular to this direction. Irrespective of this factor, lattice strains simulated with the self hardening model provides good agreement to the experimental results, shown in Fig. 11 (b).

The initial strain-ratio in Strain-Path 3 replicates Strain-Path 1. Experimentally changing the strain-ratio to biaxial deformation yields initially larger lattice strains parallel to RD compared to TD. The model predicts the lattice strain distribution remains largely unchanged with increasing stroke displacement, seen in Fig. 11 T1-C, retaining greater levels of lattice strain parallel to RD compared to TD, a feature not measured experimentally. Beyond 15 mm stroke displacement, the experimentally measured lattice strain with ψ becomes quite uniform. The differences observed are likely an artifact of the very small macroscopic strain that had accumulated during the second loading step, as shown in Fig. 11 (c). An error in measuring and particularly underestimating the macroscopic strain, that is subsequently modelled will undoubtedly result in differences in the modelled lattice strain distributions. Whilst this difference is evident, the lattice strain distribution from stroke displacement 10 mm to 15 mm immediately after the strain-path change have been well replicated, demonstrating that the CPFE simulation has successfully predicted an influence of previous straining. The simulations also predict that rotating the sheet (T1-F) provides lower absolute values of {310} lattice strain during biaxial straining (after a uniaxial pre-strain), sufficient to become compressive in RD, parallel to the tensile axis of the uniaxial pre-strain.

4.5. Development of texture and dislocations

Measurements of reflection intensity can be compared to the textures simulated by CPFEM simulations. For the {200} and {110} reflections, equivalent information was generated by extracting intensities at the perimeter of {100} and {110} pole figures calculated from modelled results. The pole figures used orientations calculated from the elastic deformation gradient extracted from each element in the model. Comparisons of normalised intensities are made in Fig. 12 at the end of the pre-strain and after the final deformation state for each of the three experimental strain-paths, with results simulated from self and isotropic hardening models. The experimental trends have some agreement with the modelled

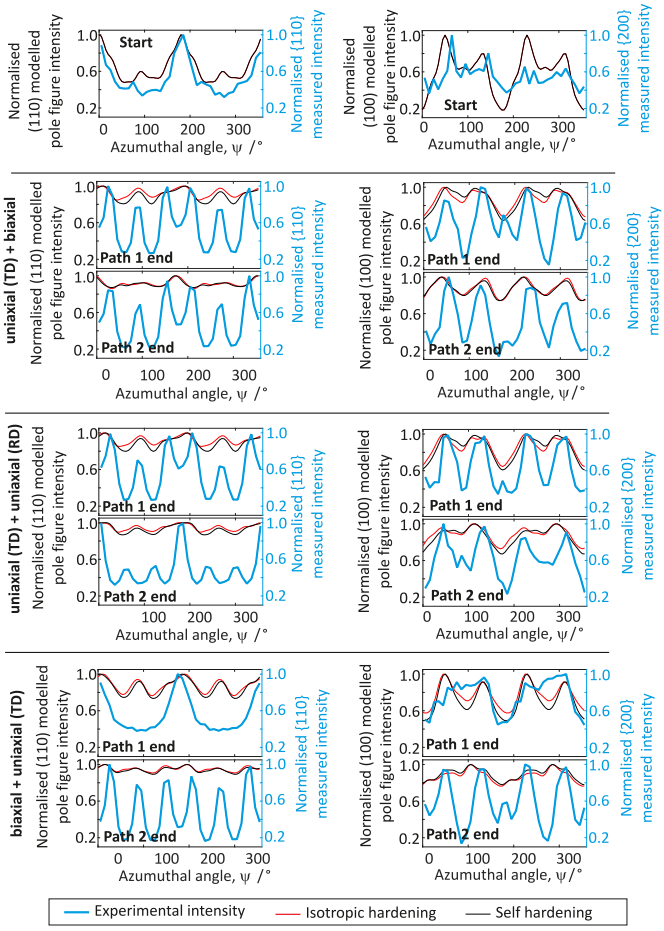

Fig. 12. Normalised experimental {110} and {200} reflection intensities compared with the normalised intensities calculated from CPFEM results for equivalent orientations to generate (100) and (110) pole figures.

results, more so for the intensities at the end of the pre-strains, (labelled Path 1 end). In each example, the change in modelled intensity between the end of Path 1 and the end of Path 2 appears to be under-predicted compared to the experiment. The under-prediction is largely an artifact from averaging orientation data from a limited number of grains, making this an expected result. The results predicted from each hardening model are similar, indicating that the different hardening rules predicted approximately the same texture change. Some success is seen when comparing points of maxima/minima in the experimental intensity and modelled pole figure intensity versus azimuthal angle. For example in the biaxial + uniaxial strain-path maxima in the {110} experimental/{110} modelled intensity, the maxima at $\psi = 0°$,180° & 360° are correctly replicated at 'Path 1 end'. Then at 'Path 2 end', the experimental maxima at approximately 30°, 80°, 150°, 210°, 280°, 330° matches the positions of the simulated intensity maxima.

Of the two hardening rules investigated using CPFEM, the self-hardening model used for lattice strain prediction had the best fidelity with the experimental results. Results from the self hardening model are considered in more detail to gain insight. Fig. 13 provides further CPFEM results obtained from the biaxial + nominally uniaxial strain path. Full pole figures during the (a) texture development, (b) the development of dislocation structures observed normal to a cross-section of the model, and (c) the distribution of stresses (given as Von Mises stress), again observed normal to the cross-section. Note that the plotted dislocation parameter, ρ is a constant obtained from the slip system strength, as given in Equations (6) and (7). Values of ρ that are output from the CPFE model are proportional to the dislocation density. Results are shown for the sheet in the experimental orientation (T1), and rotated by 90° (T2) to monitor the influence of the starting texture.

Both T1 and T2 textures show an increasingly diffuse intensity distribution as the deformation progresses (from start, end of biaxial pre-strain, then after the nominally uniaxial path). As the starting 110 texture fibre is lost, the intensity reduces as expected, instead showing localised regions of high intensity in the approximate locations labelled A. Of these four locations, all intensities except the bottom left have decreased compared to the starting pole figure. At the final deformation state after the nominally uniaxial strain-path, high intensity is seen close to locations labelled B in the T1 path, though is not so strong for the T2 texture.

Snapshots of the spatial distribution of dislocations densities are shown in Fig. 13 (b), where subtle differences between texture T1 and T2 can be seen, both after the biaxial pre-strain, after the nominally uniaxial path, and in the dislocation density difference shown in column 3 of Fig. 13 (b). This can be seen both in the maps showing 8 × 8 grains across the model and in the maps of magnified single grains. Equivalently the stress distributions in Fig. 13 (c) are quite different between the end of each deformation step, and between textures T1 and T2. The plots indicate both the inhomogeneous nature of the stress distributions across and within the grains. The distributions change significantly when the strain path is changed, and are evidently different for T1 and T2 textures.

4.6. Prediction of the ductility

Failure strain predictions from the crystal plasticity simulations using self-hardening are shown in Fig. 14. Three strain-paths were modelled; (1) a calibration strain-path for plane strain deformation, (2) uniaxial loading pre-strain, U (magnitude equal to experiment) + biaxial (along path U-d), and (3) biaxial pre-strain, B (again magnitude equal to experiment) + uniaxial (along path B-a). The simulated biaxial+nominally uniaxial strain-path failure strain is within the experimental error bars at an equivalent plastic strain $\varepsilon_{eq} = 0.53$, though the nominally uniaxial + biaxial path under predicts the total strain ($\varepsilon_{eq} = 0.59$ compared to experiment $\varepsilon_{eq} = 0.72$). However, the model does correctly predict this strain-path has the greatest strain to failure of the 3 simulated paths, replicating the result observed experimentally and capturing the large ductility benefit generated by this non-proportional deformation path.

5. Discussion

Nakajima testing is a standard method of determining the forming limit of a metallic material, where factors such as property anisotropy are not accounted for. Typically, sheet orientation is not considered, giving a random orientation of the tensile axis with respect to any prior rolling direction. The non-proportional forming limit data shown in Fig. 6 shows a uniaxial pre-strain followed by further uniaxial deformation (strain-path U-a) reaching a final plastic strain beyond the proportional forming limit. This was an unexpected result. If the testing conditions are the same, the failure of U-a should lie on the proportional forming limit curve. Sheet orientation is one variable which could give such a difference, where it is likely that the sheet orientation during this test has not been equivalent to the orientation of the sheet during proportional testing. Nakajima testing is also sensitive to strain-rate [40]. The pre-strain sheet and waisted specimens during subsequent

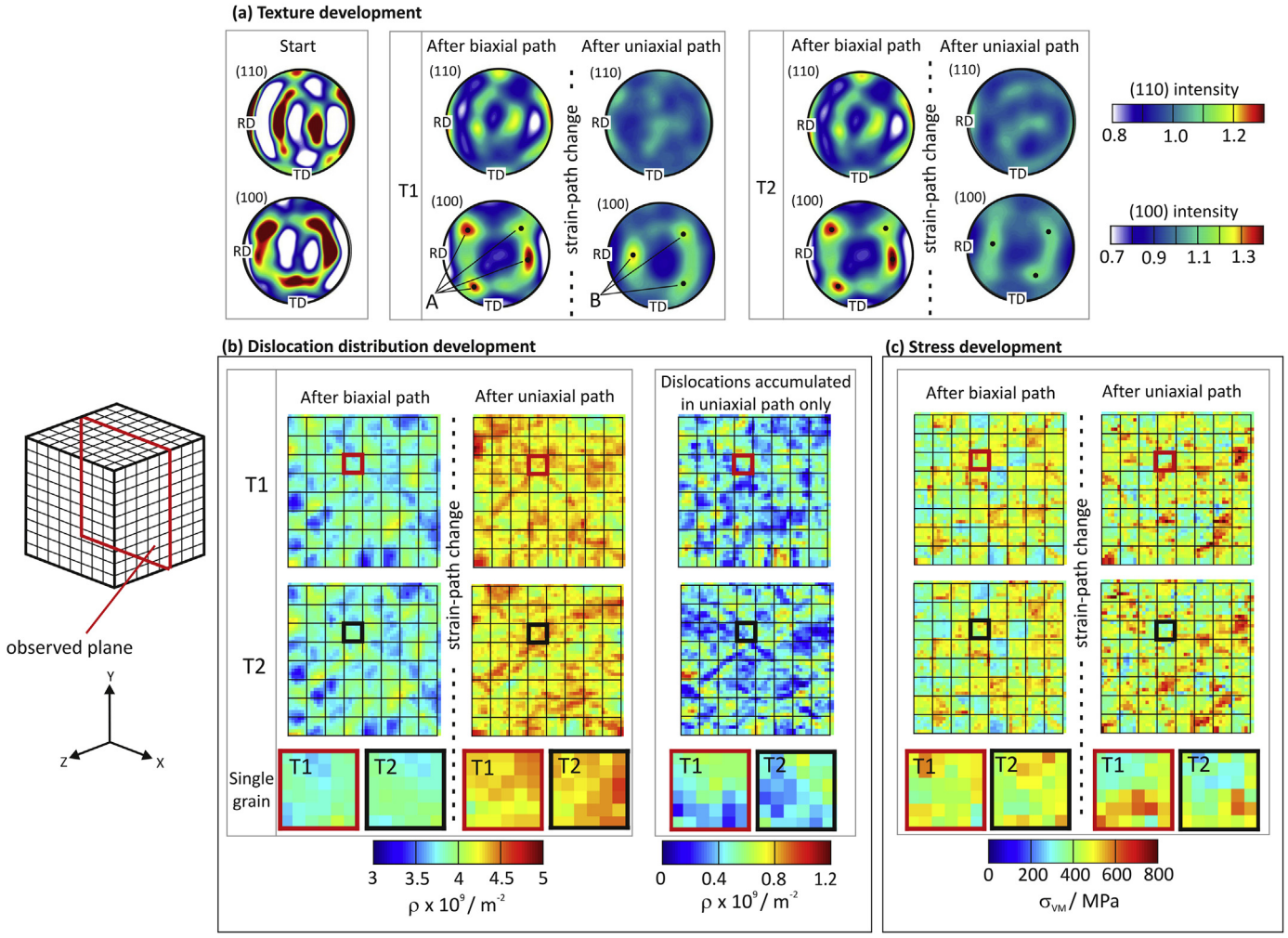

Fig. 13. Development of dislocation structures and stress fields through a plane section through the modelled polycrystal. Results are shown for the biaxial + uniaxial strain-path modelled with self hardening.

deformation have very different geometries, making it nearly impossible to have a constant strain-rate at each stage of deformation, thus affecting the final strain at failure. Strain-path U-a also deviates from perfect uniaxial loading, again due to differences between pre-strain and Nakajima testing geometries. This may further contribute to the gain in ductility. Finally macroscopic strains measured via DIC were obtained from an average area at the centre of the sample measuring approximately 2×2 mm^2. This method could overestimate the final strain by unknowingly incorporating a region that has partly necked or thinned, thus giving an overestimate of the final strain. Each strain-path was tested three times, with the data point given as the mean plastic strain and the error bars denote the scatter in the major and minor strain directions. The size of error varies from point to point, with strain-path B-a noticeably larger than others. Again, differences in sheet orientation relative to the prior rolling direction is the likely cause.

For in-situ lattice strain measurements, the macroscopic strains were smaller than the pre-strains given in the Nakajima tests. This was to mitigate the risk of not obtaining suitable data in the limited experimental time available at a synchrotron facility. Also, whilst these large strains can be measured in a Nakajima test, they are not achievable with the design of cruciform used. The design used enables the experiment to be performed, but has not been fully optimised. Each cruciform specimen was machined to the final geometry, giving a layer of cold work on the surface. Thus, it was likely that the ductility of the sample was reduced. Annealing the specimens would alleviate this problem, however, a grain size increase could not be tolerated (assuming a mean grain diameter of 20 μm, approximately 2×10^5 grains are in the diffracting volume, from which only a small fraction contribute to the diffraction signal). It is assumed that the data presented was representative of the bulk response, which would be less convincing if the number of grains through the thickness were reduced (giving rise to a different macroscopic behaviour which is more likely to be dominated by a single favorably orientated grain), in conjunction with a decay in diffraction pattern quality with a reduction in the number of grains that obey the Bragg condition within the diffracting volume.

A number of clear differences were identified from the X-ray diffraction results between non-proportional loading and proportional monotonic loading. The first is the distribution of lattice strains. Both the lattice strain distributions during biaxial and uniaxial deformation with a pre-strain (Fig. 8(i–l) & (q-t), respectively, after the strain-path change) are different to the lattice strain distributions from the same strain-ratio, but without a pre-strain (Fig. 8(q–t) & (i-l), respectively, before the strain-path change). Modelling the same strain-path twice but with the sheet rotated 90° for one simulation gives different magnitudes of lattice strain

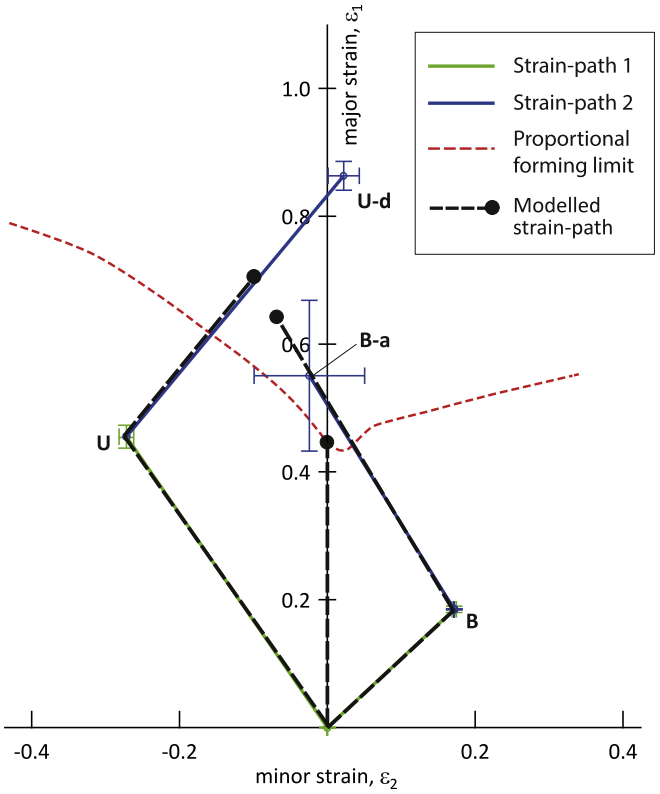

Fig. 14. Modelled failure strain predictions using a self hardening law for selected strain-paths.

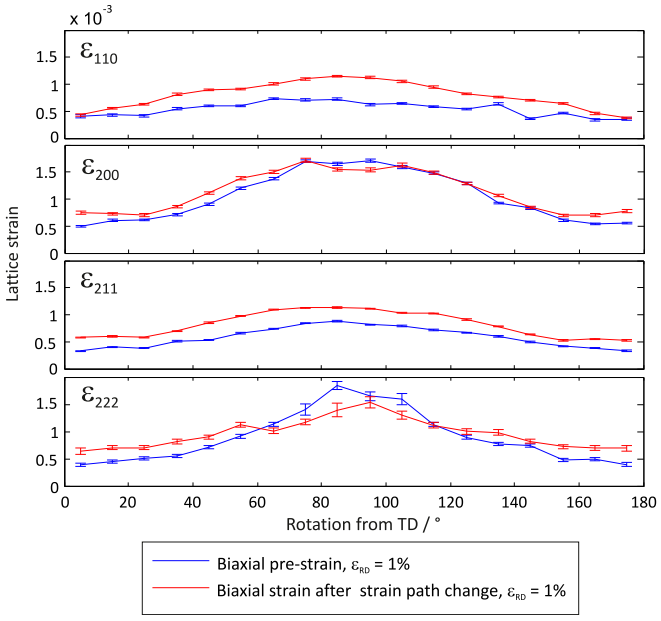

Fig. 15. Comparison of lattice strain distributions for 1% macroscopic strain (RD) during a biaxial pre-strain and 1% macroscopic strain (RD) for biaxial deformation after a uniaxial pre-strain.

with respect to ψ, indicating texture does influence the distribution of lattice strains. The modelled strain-paths T1-A and T1-D (Fig. 11), for example, had the sequence of strain switched, i.e. with uniaxial (RD) followed by uniaxial (TD) versus uniaxial (TD) followed by uniaxial (RD). Here, the magnitude of lattice strains and their distributions are different, reiterating that the sheet orientation, and hence texture, will affect the absolute lattice strains measured.

In the specific example of biaxial deformation after a uniaxial pre-strain in Strain-Path 3, the lattice strain distribution does not become isotropic (Fig. 8(q–t)), compared to a biaxial deformation pre-strain (Fig. 8(i–l)). Though the stroke displacement during Strain-Path 3 increases significantly, the macroscopic strain in the centre of the sample is limited to just 1%. To see how significantly the pre-strain may be affecting the lattice strain distributions, lattice strains as a function of rotation from the transverse direction are compared between the biaxial pre-strain at $\varepsilon_{RD} = 1\%$ and $\varepsilon_{RD} = 1\%$ after the path change in Strain-Path 3. This is shown for reflections {110}, {200}, {211} and {222} in Fig. 15. Differences are most evident for the ε_{110} and ε_{222} lattice strain distributions. Diffracting grain families with similar orientations but with higher lattice strain magnitudes have undergone more work hardening. This has been influenced by the history of the material including prior deformation and texture. This is evident at ~90° from TD where ε_{110} after the strain path change is higher than the pre-strain. This effect is not observed for all lattice planes; it is absent in the ε_{200} distribution, for example.

It has been reported that if the material is subjected to significant strain-path changes, which results in pre-strain dislocation microstructures being lost, a stagnation in work hardening may result [41]. Plotting lattice strains with macroscopic strain provided an indication of the work hardening behaviour (Fig. 10). In the strain-paths studied, there was evidence that the rate of work hardening was different in a pre-strain compared to deformation after the strain path had been changed. The most pronounced difference was observed in Strain-Path 1: uniaxial loading (RD) deformation after a uniaxial loading (TD) pre-strain, Fig. 10 (a) & (c). Work hardening appears limited in the new tensile axis (RD). However, a decreasing rate of work hardening with increased macroscopic change would be observed through proportional loading without a strain-path change. Hence, this is not an unexpected observation. Changes in lattice strain distribution are, however, evident from a change in strain-path, indicating work hardening rates have been affected. This observation, though subtle, could indicate that an altered dislocation microstructure, for example, is developing and affecting work-hardening rates, and thus generates changes in observed lattice strain distributions. Factors such as this may be key to the ductility gain observed by certain strain paths.

The second observation is the evolution of texture itself. The reflection intensities reported in Fig. 8 provide indications of the specific texture changes during deformation. Using the well known textures for a BCC material, a ⟨110⟩ fibre develops during uniaxial deformation and mixed ⟨100⟩ and ⟨111⟩ fibres develop during uniaxial compression [42]. For the latter case, this fibre texture is also observed during biaxial deformation [20]. The fibre textures that develop after a pre-strain were not shown to be any different to those that develop without a pre-strain. In all cases, the observed fibre textures were exactly as expected for either uniaxial or biaxial deformation. There was also no evidence that the pre-strain texture was retained for any significant period of plastic strain once the strain-path was changed. Texture changes due to a strain-path change have been reported to directly affect the macroscopic stress-strain response [43]. This observation has not been repeated by this study. With few strain-paths studied experimentally, the strength of the texture itself and the influence upon lattice strain distributions cannot yet be measured. However, the evolution of modelled texture for a biaxial+uniaxial strain-path presented as pole figures in Fig. 13 showed that the strength of texture does decay, i.e. the orientation spread within the material becomes more

isotropic after a change in strain-path. The result would undoubtedly influence the accumulation and distribution of dislocations as the material is deformed further.

CPFE modelling in this study indicates that the magnitudes of lattice strains that develop are dependent on two key criteria. (1) The orientation of the tensile axes relative to pre-existing fibre textures; influencing both the pre-strain and further deformation following a strain path change. (2) The strain ratio of the pre-strain will affect the distributions of lattice strains developing during any further deformation. The simulations demonstrate the important need for further investigations to study the sensitivity of a strain-path to the orientation of the sheet. The simulation results provide qualitative indications of differences which may be expected from different strain-paths, and success is seen for the prediction of {310} lattice strains. Some differences are, however, expected from the simulated diffraction data generated from relatively few grains (512) compared to the experiment ($>2 \times 10^5$ in diffracting volume), necessitating the averaging of grains over a wider orientation range than experimentally acquired [26]. Evidence from lattice strain measurements of different work hardening rates between pre-strain deformation and deformation following a strain path change suggests that pre-existing dislocations structures are likely to influence subsequent deformation, which may not be accounted for by the hardening rules used in this study.

Rauch and Schmitt [44] postulated that during deformation after a path-change, new dislocation structures form, such as microbands or cell wall boundaries. These must interact, dissect and eventually replace any pre-excisting structure. Whilst details of the dislocation structures have not been measured in this study, this is certainly of interest in future work to inform constitutive laws that capture hardening more precisely. Modelled maps of dislocation density distributions shown in Fig. 13 demonstrate that subjecting the material to the same biaxial+uniaxial deformation, but with the steel sheet rotated, gives different structures accumulating between a pre-strain and after a strain-path change. The organisation of dislocations is likely a key governing mechanism for the differences in work hardening rates between a pre-strain and deformation following a strain-path change.

The CPFE modelling results demonstrated that a self-hardening model provides good fidelity between experimentally measured and predicted lattice strains. The work hardening rates were well replicated, whereas isotropic latent hardening overestimated this, predicting lattice strains far higher than those measured experimentally. The failure of isotropic hardening and success of self-hardening indicates that the hardening of each slip system is independent. This method captures the history of each slip system, enabling them to harden at rates governed by their independent resistance to slip. A change in strain-path results inevitably in a change to the microscopic stress state, and thus affecting which slip systems are active. Forcing slip systems to harden at the same rate underestimates the total accumulated slip, increasing microscopic stress and hence the calculated lattice strains. It was observed that the lattice strain distributions provided a better discriminator of the material constitutive laws than the texture development.

The motivation for in-situ observations during non-proportional deformation was to give insight into strain-paths that display a ductility gain when measured with Nakajima testing, particularly for uniaxial deformation followed by biaxial straining. CPFE simulations that incorporated a self hardening rule were used to predict the failure strain of selected Nakajima tests where ductility gains were observed. The model successfully identified a ductility gain for non-proportional strain-paths and moreover correctly predicted that uniaxial + balanced biaxial deformation has a greater strain to failure than balanced biaxial + uniaxial. The failure criterion is based on the localisation of strain, indicating that the uniaxial + biaxial strain-path homogeneously distributes plasticity for a larger macroscopic strain than the other strain paths studied.

6. Summary

1. A novel high energy X-ray diffraction experiment has shown, for the first time, the micromechanical response of metallic cruciform specimens, in-situ, during non-proportional deformation.
2. A significant ductility gain is observed via Nakajima testing when subjecting a low carbon ferritic steel to a non-proportional strain-path. Whilst a uniaxial pre-strain followed by biaxial deformation provides a significant strain to failure gain compared to plane-strain proportional deformation, a biaxial pre-strain provides no such ductility gain, or in the worst case, can be detrimental to ductility.
3. The accumulation of lattice strain with respect to azimuthal angle is shown to be sensitive to the applied strain-ratio. Moreover, this lattice strain distribution for certain lattice planes is influenced by the strain-ratio of the pre-strain. A lower work hardening rate after the pre-strain in the direction of the largest tensile axis was observed, however, this is not unique to a non-proportional deformation, as work hardening rates would tend to reduce with increasing macroscopic strain for proportional loading.
4. Observation of the intensity change throughout deformation indicates that new texture fibers develop when a strain-path is changed. The texture fibres that develop were not shown to be influenced strongly by the pre-strain.
5. Simulation of Debye-Scherrer diffraction patterns has been performed from CPFE modelling of various non-proportional strain paths, providing lattice strains throughout the deformation. Two constitutive laws were considered namely; self and isotropic latent hardening, the former was found to better replicate the lattice strain variations measured experimentally.
6. CPFE models that incorporated self-hardening were used to simulated the failure strain of selected non-proportional strain paths identified from Nakajima testing. The models were successful in replicating the non-proportional ductility gain and correctly identified a path with a uniaxial pre-strain has the highest strain to failure.

Acknowledgments

Funding has been provided by EPSRC (grant EP/I021043/1) with material and guidance from BMW-MINI gratefully acknowledged. With thanks also to the Diamond Light Source for the allocation of beamtime EE9333-1 on the I12 instrument and to Hamidreza Abdolvand for his assistance during the experiment. Datasets from this manuscript will be made available via the Oxford University Research Archive (ora.ox.ac.uk).

References

[1] K. Nakazima, T. Kikuma, K. Hasuka, Study on the Formability of Steel Sheets, Technical Report 264, Yawata Technical, 1968, pp. 8517–8530.
[2] M. Zandrahimi, S. Platias, D. Price, D. Barrett, Effects of changes in strain path on work hardening in cubic metals, Metall. Trans. A 20 (1989) 2471–2482.
[3] A. Ghosh, W. Backofen, Strain hardening and instability in biaxially stretched sheets, Metall. Trans. 4 (1973) 1113–1123.
[4] A. Graf, W. Hosford, Calculations of forming limit, Metall. Trans. A 24 (1993) 2503–2512.
[5] S. Keeler, W. Backofen, Plastic instability and fracture in sheet stretched over rigid punches, ASM Trans. Q. 56 (1963) 25–48.
[6] D. Banabic (Ed.), Formability of Metallic Materials: Plastic Anisotropy, Formability Testing, Springer, 2000.
[7] R. McGinty, D. McDowell, Application of multiscale crystal plasticity models to forming limit diagrams, J. Eng. Mater. Technol. 126 (2004) 285–291.
[8] A. Doucet, R. Wagoner, Transient tensile behavior of interstitial-free steel and

70/30 brass following plane-strain deformation, Metall. Trans. A 20 (1989) 1483–1493.
[9] Z. Hu, E. Rauch, C. Teodosiu, Work-hardening behavior of mild steel under stress reversal at large strains, Int. J. Plast. 8 (1992) 839–856.
[10] B. Peeters, S. Kalidindi, P. Van Houtte, E. Aernoudt, A crystal plasticity based work-hardening/softening model for b.c.c. metals under changing strain paths, Acta Mater. 48 (2000) 2123–2133.
[11] S. Thuillier, E. Rauch, Development of microbands in mild steel during cross loading, Acta Metall. Mater. 42 (1994) 1973–1983.
[12] R.K. Verma, T. Kuwabara, K. Chung, A. Haldar, Experimental evaluation and constitutive modeling of non-proportional deformation for asymmetric steels, Int. J. Plast. 27 (2011) 82–101.
[13] T. Erinosho, A. Cocks, F. Dunne, Coupled effects of texture, hardening and non-proportionality of strain on ductility in ferritic steel, Comp. Mater. Sci. 80 (2013) 113–122.
[14] T. Erinosho, A. Cocks, F. Dunne, Texture, hardening and non-proportionality of strain in BCC polycrystal deformation, Int. J. Plast. 50 (2013) 170–192.
[15] M. van Riel, A. van den Boogaard, Stress-strain responses for continuous orthogonal strain path changes with increasing sharpness, Scr. Mater. 57 (2007) 381–384.
[16] J. Repper, M. Niffenegger, S.V. Petegem, W. Wagner, H.V. Swygenhoven, In Situ biaxial mechanical testing at the neutron time-of-flight diffractometer POLDI, Mat. Sci. Forum 768–769 (2013) 60–65.
[17] S.V. Petegem, J. Wagner, T. Panzner, M. Upadhyay, T. Trang, H.V. Swygenhoven, In-situ neutron diffraction during biaxial deformation, Acta Mater 105 (2016) 404–416.
[18] D. Gonzalez, J. Kelleher, J.Q. da Fonseca, P. Withers, Macro and intergranular stress responses of austenitic stainless steel to 90° strain path changes, Mater. Sci. Eng. A 546 (2012) 263–271.
[19] T. Marin, P. Dawson, M. Gharghouri, R. Rogge, Diffraction measurements of elastic strains in stainless steel subjected to in situ biaxial loading, Acta Mater 56 (2008) 4183–4199.
[20] D. Collins, M. Mostofavi, R. Todd, T. Connolley, A. Wilkinson, A synchrotron X-ray diffraction study of in situ biaxial deformation, Acta Mater 90 (2015) 46–58.
[21] T. Foecke, M. Iadicola, A. Lin, S. Banovic, A method for direct measurement of multiaxial stress-strain curves in sheet metal, Metall. Mater. Trans. A 38 (2007) 306–313.
[22] M. Iadicola, T. Foecke, S. Banovic, Experimental observations of evolving yield loci in biaxially strained AA5754-O, Int. J. Plast. 24 (2008) 2084–2101.
[23] Y. Jeong, M. Iadicola, T. Gnäupel-Herold, A. Creuziger, Multiaxial constitutive behavior of an interstitial-free steel: measurements through x-ray and digital image correlation, Acta Mater 112 (2016) 84–93.
[24] C. Wejdemann, H.F. Poulsen, U. Lienert, W. Pantleon, The effect of strain path change on subgrain volume fraction determined from in situ X-ray measurements, IOP Conf. Ser. Mater. Sci. Eng. 3 (2009) 012003.
[25] M. Upadhyay, S.V. Petegem, T. Panzner, R. Lebensohn, H.V. Swygenhoven, Study of lattice strain evolution during biaxial deformation of stainless steel using a finite element and fast fourier transform based multi-scale approach, Acta Mater 118 (2016) 28–43.
[26] T. Erinosho, D. Collins, A. Wilkinson, R. Todd, F. Dunne, Assessment of x-ray diffraction and crystal plasticity lattice strain evolutions under biaxial loading, Int. J. Plast. 83 (2016) 1–18.
[27] BMW AG Group Standard, Cold-rolled DP Steels (GS 93005-11), 2009. Technical Report.
[28] Cold-rolled DP Steels, BMW AG, 2009. Technical Report GS 93005-11.
[29] M. Drakopoulos, T. Connolley, C. Reinhard, R. Atwood, O. Magdysyuk, N. Vo, M. Hart, L. Connor, B. Humphreys, G. Howell, S. Davies, T. Hill, G. Wilkin, U. Pedersen, A. Foster, N. De Maio, M. Basham, F. Yuan, K. Wanelik, I12: the joint engineering, environment and processing (JEEP) beamline at Diamond Light Source, J. Synchrotron Radiat. 22 (2015) 828–838.
[30] M. Hart, M. Drakopoulos, C. Reinhard, T. Connolly, Complete elliptical ring geometry provides energy and instrument calibration for synchrotron-based two-dimensional X-ray diffraction, J. Appl. Cryst. 46 (2013) 1249.
[31] FIT2D, http://www.esrf.eu/computing/scientific/FIT2D/, Accessed March 2014.
[32] M. Mostafavi, D. Collins, B. Cai, R. Bradley, R. Atwood, C. Reinhard, Yield behavior beneath hardness indentations in ductile metals, measured by three-dimensional computed x-ray tomography and digital volume correlation, Acta Mater 82 (2015) 468–482.
[33] E. Lee, Elastic-plastic deformation at finite strains, J. Appl. Mech. 36 (1969) 1–6.
[34] D. Peirce, R. Asaro, A. Needleman, Material rate dependence and localized deformation in crystalline solids, Acta Metall. 31 (1983) 1951–1976.
[35] Y. Huang, A User-material Subroutine Incorporating Single Crystal Plasticity in the Abaqus Finite Element Program, Harvard University Report, MECH 178, 1991. Technical Report.
[36] T. Erinosho, D. Collins, A. Wilkinson, R. Todd, F. Dunne, The Role of Statistics in CPFE/diffraction Simulations, 2016. In Preparation.
[37] W. Volk, P. Hora, New algorithm for a robust user-independent evaluation of beginning instability for the experimental flc determination, Int. J. Mater. Form. 4 (2011) 339–346.
[38] Q. Situ, M. Jain, D. Metzger, Determination of forming limit diagrams of sheet materials with a hybrid experimental-numerical approach, Int. J. Mech. Sci. 53 (2011) 707–719.
[39] J. Nye, Physical Properties of Crystals, Oxford University Press, 1957.
[40] W. Volk, P. Hora, Evaluation of experimental forming limit curves and investigation of strain rate sensitivity for the start of local necking, AIP Conf. Proc. 1383 (2011) 99–106.
[41] E. Nesterova, B. Bacroix, C. Teodosiu, Microstructure and texture evolution under strain-path changes in low-carbon interstitial-free steel, Metall. Mater. Trans. A 32 (2001) 2527–2538.
[42] U. Kocks, C. Tomé, H.-R. Wenk, Texture and Anisotropy, Cambridge University Press, Cambridge, UK, 1998.
[43] B. Bacroix, Z. Hu, Texture evolution induced by strain path changes in low carbon steel sheets, Metall. Mater. Trans. A 26 (1995) 601–613.
[44] E. Rauch, J. Schmitt, Dislocation substructures in mild steel under monotonic loading conditions and cross-loading, Mater. Sci. Eng. A 113 (1989) 441–448.